

Auxetic dihedral Escher tessellations

Xiaokang Liu ^a, Lin Lu ^{a,*}, Lingxin Cao ^a, Oliver Deussen ^b, Changhe Tu ^a

^a School of Computer Science and Technology, Shandong University, Qingdao, China

^b Computer and Information Science, University of Konstanz, Konstanz, Germany

ARTICLE INFO

Keywords:

Auxetic structure design
Rotating (semi-)rigid structure
Deployability optimization

ABSTRACT

The auxetic structure demonstrates an unconventional deployable mechanism, expanding in transverse directions while being stretched longitudinally (exhibiting a negative Poisson's ratio). This characteristic offers advantages in diverse fields such as structural engineering, flexible electronics, and medicine. The rotating (semi-)rigid structure, as a typical auxetic structure, has been introduced into the field of computer-aided design because of its well-defined motion patterns. These structures find application as deployable structures in various endeavors aiming to approximate and rapidly fabricate doubly-curved surfaces, thereby mitigating the challenges associated with their production and transportation. Nevertheless, prior designs relying on basic geometric elements primarily concentrate on exploring the inherent nature of the structure and often lack aesthetic appeal. To address this limitation, we propose a novel design and generation method inspired by dihedral Escher tessellations. By introducing a new metric function, we achieve efficient evaluation of shape deployability as well as filtering of tessellations, followed by a two-step deformation and edge-deployability optimization process to ensure compliance with deployability constraints while preserving semantic meanings. Furthermore, we optimize the shape through physical simulation to guarantee deployability in actual manufacturing and control Poisson's ratio to a certain extent. Our method yields structures that are both semantically meaningful and aesthetically pleasing, showcasing promising potential for auxetic applications.

1. Introduction

Auxetic structures are characterized by a property known as negative Poisson's ratio (NPR). Traditional auxetic structures include re-entrant, chiral, perforated, and rotating (semi-)rigid structures. Compared to re-entrant and chiral structures, the rotating structure demonstrates clearer kinematics, with each unit rotating around the connection point under external forces, resulting in a uniform expansion effect across the entire structure, as illustrated in Fig. 1. This characteristic affords a controlled range of properties, rendering rotating structures versatile for various applications. Additionally, the perforated structure can be considered a special type of rotating structure, allowing researchers to manipulate its mechanical properties by adjusting the slit shape and position.

In recent years, with advances in materials science and digital fabrication, attention has been poured into creative design explorations based on easily controllable rotating (semi-)rigid structures. From the investigation of the properties of different rotational structures based on various polygons [1–7] to the generation of a variety of customized complex 2D structures [8,9] and 3D surfaces [10–15] based on designed rotating (semi-)rigid structures.

However, these structures often rely on the rotation of basic geometric elements, such as parallelograms and rhombuses, which also present significant design opportunities, particularly in the realm of custom design and manufacturing.

This paper delves into the exploration of introducing meaningful contours to the fundamental units of rotating structures, enhancing their visual appeal and creating a sense of intuitive aesthetics. Specifically, we aim to characterize these structures in their compact state as dihedral Escher tessellations, where the intricate patterns, symmetries, and dual figure-ground arrangements evoke fascination and challenge conventional visual perception and categorization. By incorporating these captivating patterns into the compact form of auxetic structures, we not only enhance their aesthetic value but also explore the fascinating interplay between form and perception.

This introduces two primary challenges. Firstly, significant features of the input shapes may impede the smooth rotation process when the basic units are deployed. Secondly, the frame formed by the connections between the units may deviate from regularity, potentially leading to issues with deployment and maintaining structural integrity, as shown in Fig. 2. Overcoming these challenges necessitates the development of novel methods to optimize the profile of these structures.

* Corresponding author.

E-mail address: llu@sdu.edu.cn (L. Lu).

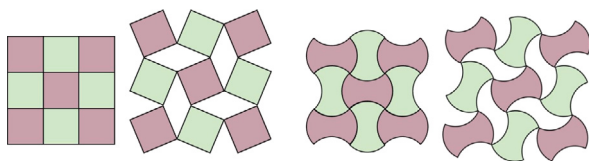


Fig. 1. Two examples of rotating (semi-)rigid structures.

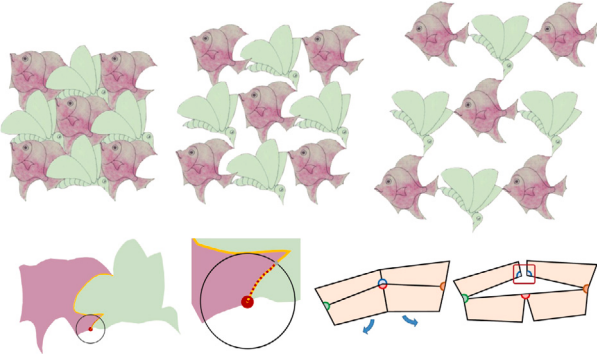


Fig. 2. Top row: An unsuccessful attempt to deploy a “fish and butterfly” dihedral tessellation. Bottom row: Two challenges faced by rotational deployable structures: (1) Features that convey the shape’s meaning may impede the rotation process upon deployment of basic units; (2) The frame formed by hinge points connecting the units is irregular and may not remain intact after deployment.

This optimization process involves leveraging a metric function that takes into account both the rotational degrees of freedom and shape semantics. The goal is to strike a delicate balance between aesthetic appeal and deployability.

Our algorithm takes as input a given dihedral Escher tessellation or a single shape (calculating its corresponding dihedral tessellation) and conducts deformation optimizations based on this tessellation. Then we deform and optimize the contour using the aforementioned metric function to generate a manufacturable shape with practical utility.

Our contributions can be summarized as follows.

- We introduce the concept of auxetic dihedral tessellation based on rotating (semi-)rigid structure with clear unit shapes, which can be deployed into a target developable surface through actuation.
- We propose an algorithm and a corresponding framework that deform given dual shapes to create a deployable dihedral Escher tessellation.
- We define a deployability metric function for this rotational structure and propose a deployability optimization method based on this function.

2. Related work

2.1. Auxetic structures

Traditional auxetic mechanical structures comprise many different types including re-entrant structures [16], chiral structures [17,18], rotating (semi-)rigid structures [1] and perforated structures [19]. Grima et al. [1–5,7] explored different kinds of rotational structures based on various polygons, conducted a theoretical analyses and discussed the relationship between different deployment methods, structural parameters and corresponding metamaterial properties. Choi et al. [8] proposed an inverse design framework to generate a compact reconfigurable and rigid deployable Kirigami patterns for a given a target shape. Warisaya et al. [9] provided topological variations of corner-connected kinematic tiling to generate novel auxetic structure based on irregular and aperiodic rhombic tiles. Attard [20] and Li et al. [21]

explored meta-materials composed of three-dimensional units and the resulting material properties. Gatt et al. [22] extended hierarchical rotating structure in order to obtain additional benefits of a hierarchy while retaining the properties of a negative Poisson’s ratio.

Grima et al. [19,23] extended rotating rigid units into perforated structures using a similar mechanism, containing diamond, star or triangular-shaped perforated sheets that exhibit auxetic behavior for tension and compression. Slann et al. [24], Pagliocca et al. [25] and Morvaridi et al. [26] investigated the impact of various perforation parameters on material properties. Mizzi et al. [27] and Shan et al. [28] introduced slit perforations within sheets or blocks of material, adjusting slit parameters to create auxetic systems with diverse behaviors.

2.2. Deployable surfaces

In the last few years, the focus of research has shifted to inverse design optimization approaches which transform or assemble fabricated components to produce a target design surface. This is a very interesting but simultaneously challenging computational problem, since its solution usually depends heavily on the material behavior of the individual components and the way how they are connected together to form a flexible and deployable structure.

Konakovic et al. [10,11], Rao et al. [12], and Jiang et al. [13] developed novel deployable structures that can be deployed from two-dimensional flat sheets, using slits or perforations, to three-dimensional shapes via inflation or gravitational loading. Inspired by ancient geometric motifs, Rafsanjani et al. [14] proposed bistable mechanical meta-materials that exhibit auxeticity and are able to keep stable in a specific deployment. Chen et al. [15] improved this work by enabling bistable structures to be deployed into 3D surfaces. Schüller et al. [29] introduced the concept of a “zipper”, which can rapidly form a target 3D object by zipping up the boundaries. Ren et al. [30] proposed an optimization-based method to generate planar curved ribbons to weave smooth freeform shapes.

In beam structure research, Panetta et al. [31] introduced the “x-shell”, an assembly of elastic deployable beams with rotational joints. Pillwein et al. later developed the elastic geodesic grid structure for easy-to-fabricate bent lamellas from a planar setup [32]. They enhanced this with patch-based grids for high local curvature features [33] and computational methods for planarity [34]. Jiang et al. [35] and Liu et al. [36] delved into quadrilateral grids for freeform buildings. Other innovations include deployable scissor linkages [37] and umbrella meshes [38] to approximate diverse freeform shapes.

The above work has mainly focused on calculating the ability to approximate surfaces of the whole structure and its kinematic mechanism, without considering adding shapes with aesthetic properties to the structure.

2.3. Escher tessellations

In recent decades, tessellations have become pivotal in artistic expression, comprising repeating shapes without gaps or overlaps. Notably, Dutch artist and mathematician M.C. Escher’s works—distinguished by intricate patterns, symmetries, and dual figure-ground compositions—have profoundly influenced the field [39]. His creations highlight visual perception ambiguities, intriguing computer graphics enthusiasts.

Dress [40] presented a class of dihedral Escher tiling, “Heaven and Hell patterns”, while Grünbaum and Shephard [41] outlined the underlying mathematics. Kaplan and Salesin [42] coined “Escherization” in computer graphics and later detailed a method for “dihedral Escherization” [43]. Koizumi and Sugihara [44] approached Escher tiling as a maximum eigenvalue problem. In contrast, Nagata and Imahori [45] integrated an energy function with an as-rigid-as-possible

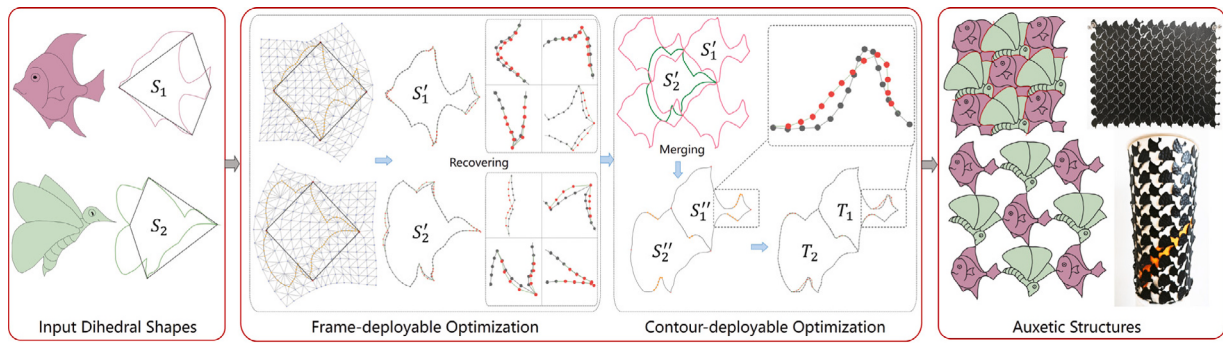


Fig. 3. Starting with the dual shapes of a dihedral tessellation, we first deform them separately using a two-step ARAP-based deformation method to transform their anchor frames into a regular geometric unit (here a rhombus). Then, we merge the two shapes and perform a deployability optimization based on a deployability metric function to obtain the final deployable dihedral Escher tessellation.

(ARAP) deformation scheme. Dual shape Escher tilings [46] focused on enhancing shape perception, and Lin et al. [47] combined matching and warping for Escher-like transformations.

Fabricable Escher tiles aim at being assembled practically: Yen and Séquin [48] devised a method for Escher tiling on a spherical domain. Howison and Séquin [49] explored 2.5D isohedral tilings via extrusion and mesh editing and crafted 3D versions using predefined lattices. Similarly, Liu et al. [50] generated printable tiles, leveraging solid and void areas. Unlike these studies that focus solely on shape constraints, our work also addresses the rotational freedom during deployment.

3. Overview

The auxetic dihedral Escher tessellation generation problem can be formulated as follows. Given target close patterns S_1 and S_2 , we compute T_1 and T_2 , so that:

1. T_1, T_2 are “mutual surrounded”, and can tile the entire plane without any gap or overlap;
2. T_1, T_2 can rotate and expand without obstructing each other;
3. T_1, T_2 and S_1, S_2 are as similar as possible.

The first two constraints ensure that the target structure can be driven to expand from a closed, undeployed state in the plane to a deployed state. The third one ensures that the result retains the contour features of the target shapes, preserving their aesthetic and interesting properties.

The *mutual surroundings constraint* [50] refers that each unit is surrounded by units of the other type and only connect to its own kind through four points. To facilitate the description of the whole algorithmic process, these four connecting points of one unit are termed as *anchor points*, and the frame formed by these points is called the *anchor frame*. In this paper, the anchor frame is limited to a quadrilateral since it have more segments and designing freedom to fit complex input patterns with less deformation than triangles.

To ensure that the meaningful shapes rotate without obstructing and the entire structure can deploy under the forces on the sides, our structure must adhere to the “*deployable constraints*”, including *frame-deployable constraint* and *contour-deployable constraint*.

The *frame-deployable constraint* mandates that each shape’s anchor frame be regular, such as a parallelogram, rectangle, rhombus, or square. In rotating structures, for successful expansion at a four-unit intersection, the sum angles of adjacent anchor frames must total 180°. Non-compliance risks deployment issues or fractures due to alignment conflicts, as shown in Fig. 2. Given the shape’s periodicity, the anchor frame should at least be a parallelogram.

The other is *contour-deployable constraint*. The anchor points divide the contour into four segments, and based on the kinematic motion of our structure, we can infer that adjacent shapes deploy around a shared rotation axis (anchor point) from their shared edge segment. For

a point on a segment, its rotating path is a circle centered on the axis of rotation with the distance between this point and the circle center as the radius. If there are two or more intersections between this path and the edge segment, it indicates that on the forward rotational path of this point, there exists points of a neighboring unit, and they will obstruct each other. Thus, the *contour-deployable constraint* requires that on the forward path of each point on edge segment, there are only points belonging to the same unit, so that to ensure unobstructed rotation.

Based on the above constraints, we design a deployability metric function and a pipeline for the generation of the auxetic structure as shown in Fig. 3. Our algorithm takes an existing Escher dihedral tessellation consisting of two shapes, denoted as S_1 and S_2 , as the input. Alternatively, one can also input a single pattern and then employ the algorithm described in [50] to generate an initial dihedral Escher tessellation as the input. Subsequently, we employ a two-step deformation optimization process for the dual shapes S'_1 and S'_2 . Firstly, we deform them using the ARAP (as-rigid-as-possible) method [51] to ensure that their anchor frames are deformed to fit a regular template. Next, we merge the two shapes and perform deployability optimization based on our deployability metric. This optimization process allows us to obtain the final dual shapes, denoted as T_1 and T_2 .

4. Technical details

In this section, we will sequentially introduce our deployability metric function and the subsequent steps of deforming and optimizing based on this function in detail.

Beforehand, anchor points are initialized according to the arrangement of the two types of shapes in the input dihedral Escher tessellation. Each shape is represented by a point set with N points (in this paper, N is 100), where the points connecting each shape to its four counterparts are noted as anchor points. Once the anchor points are determined, the subsequent distance calculation is also determined.

4.1. Deployability metric

Our deployability metric consists of two components, frame-deployable distance (FDD) and contour-deployable distance (CDD), corresponding to the frame-deployable constraint and the contour-deployable constraint, respectively.

Frame-deployable distance (FDD). FDD describes the minimum distance between the anchor frame and the regular deployable template. Based on the previous definitions, it is known that only if the anchor frame is a regular geometric shape, can such rotating (semi-)rigid structures be ensured to deploy without obstruction, deformation, or buckling. Therefore, the FDD is defined as the minimum consumption required to deform the current irregular anchor frame to a regular shape.

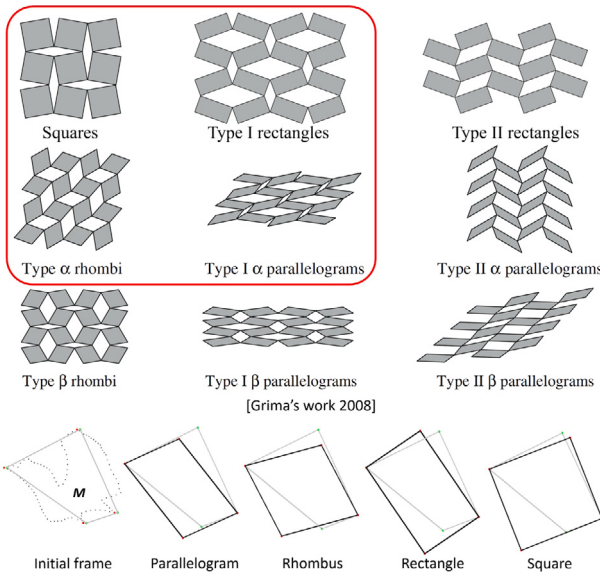


Fig. 4. Building upon [5], we selected four viable templates and their respective deployment methods. Then we computed the deviation between the target framework and these templates, selecting the one with the smallest error.

Grima et al. [5] introduced nine deploying methods for four types of regular units. Type I systems have the characteristic of always having a rhombus-shaped empty area between the shape units, while Type II systems do not. The α -type represents a system made from rhombus having their smaller angle attached with the larger angle of adjacent rhombus, while the β -type represents a system with rhombus having their smaller angle attached with the smaller angle of adjacent rhombus and the larger angle being attached with the larger angle.

It is worth noting that in Type II structures, when they are in a tightly contracted state, the long edge of the unit is always aligned with a short edge and a portion of another long edge. The high degree of coupling of the boundaries makes it difficult to design shapes for the units of a structure with such kinematic mode. Type β structures do not achieve a fully tiled state when they are undeployed. Therefore, four types of geometric elements, squares, rectangles, rectangles and parallelograms, and their corresponding four deploying methods are retained as the deployable templates for this paper, as shown in red box in Fig. 4.

For a pattern S , $FDD(S)$ describes the minimum distance between its anchor frame S^f , and the regular geometric template, whose shape parameters need to be calculated first. Here we introduce how to determine a corresponding template shape S^t for a given template type by controlling the anchor point movement:

1. Parallelogram: fix one pair of relative anchor points and move another pair of relative anchor points so that the diagonals are equal to each other.

2. Rhombus: rotate the diagonals so that they are perpendicular to each other.

3. Rectangle: extend the short diagonal so that it is equal to the other one.

4. Square: do not require additional calculations.

Then, we use Procrustes analysis to align four different templates with anchor frame S^f respectively. Procrustes analysis is a common tool in statistics and shape analysis to align shapes by means of translation, scaling, and rotation. For a shape composed of (p_1, p_2, \dots, p_N) , first aligned with another shape's centroid by translating its centroid \bar{p} . The two shapes are then scaled so that the root mean square distance $s = \sqrt{\frac{\sum_{i=1}^N (p_i - \bar{p})^2}{N}}$ is equal. When rotating, one shape is fixed as the reference direction, the other shape is rotated around the center of

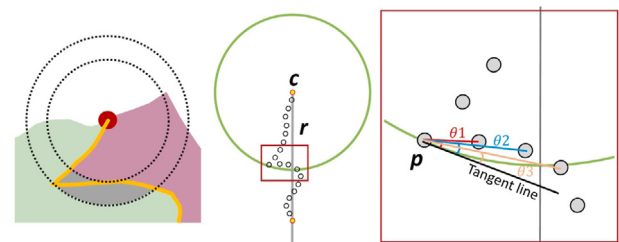


Fig. 5. As the edge rotates around center c , point p moves along the green path, which is the circle centered at c with a radius r . There are three points that collide with p . We calculate in turn the angle of their connecting line to the tangent line at point p and regard the sum of the angles of all pairs of collided points as the deployability of this edge.

mass, and then traverse all angles to find the optimal rotation angle that minimizes the sum of the squared distances (Euclidean distances) between the corresponding points. The minimum value can be used as a statistical measure of the difference between the two shapes, often also referred to as Procrustes distance (PD) :

$$PD(A, B) = \sqrt{\sum_{i=1}^N |p_{Ai} - p_{Bi}|^2} \quad (1)$$

We calculates the PD between four template shapes and anchor frame and find the most similar template S_{min}^t with minimum PD. Then the ratio of $PD(S^f, S_{min}^t)$ to the perimeter of S^f is denoted as $FDD(S)$:

$$FDD(S) = \frac{PD(S^f, S_{min}^t)}{\text{Perimeter}(S^f)} \quad (2)$$

Contour-deployable distance (CDD). CDD describes the minimum consumption required to optimize an arbitrary contour to be deployable. If a contour shape is defined as *deployable*, then the rotation path of each point on the edge segment just have one intersection with this segment, otherwise the unit will inevitably be obstructed with neighboring unit during deploying. As shown in the left of Fig. 5, the gray areas of two adjacent units obstruct each other from rotating.

The area of the gray can reflect the consumption of optimizing a shape into a deployable to a certain extent, but sometimes different shapes having the same area face completely different optimization difficulties. Therefore, in this paper, we consider evaluating the consumption of optimization through the geometric positional relationship of points.

As shown in Fig. 5, for each point p_i on the edge, check if there is an **obstructed point** $p_{i+t}, t > 0$ within the circular rotation path of p_i , and if so, compute the angle $\theta_{(i,i+t)} < 90^\circ$ between the line segment p_ip_{i+t} and the tangent line of p_i . The p in the case shown in Fig. 5 has three obstructed points. Calculate the corresponding angles of these three points, and the sum is denoted as the contour-deployable distance of point p . Subsequently, the entire edge is traversed and the value of all points is computed to obtain the contour-deployable distance of the edge e . Since the contour of shape S is divided into four segments by four anchor points, the $CDD(S)$ can be further defined as:

$$CDD(S) = \sum_{j=1}^4 \sum_{i=1}^{N_{e_j}} \sum_{k=1}^{N_{p_i}} \frac{|\theta_k|}{\pi N_{p_i}} \quad (3)$$

Here, N_{p_i} is the number of obstruction points encountered by point p_i , θ_k is the angle between the line connecting p_i and the k th obstruction point and the tangent line, and N_{e_j} denotes the number of points on side e_j .

Based on the above two metrics, we can obtain the deployability score $DepDis$ for shape S as:

$$DepDis(S) = FDD(S) + CDD(S) \quad (4)$$

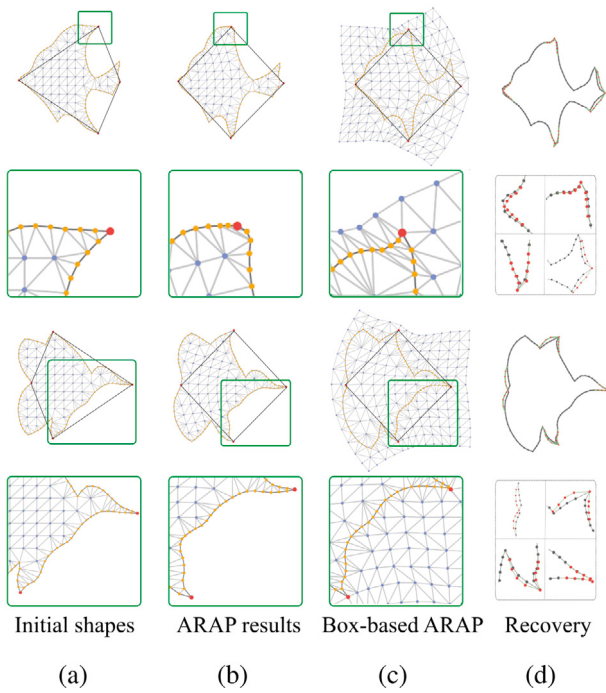


Fig. 6. Column (a) shows a triangulation after adding points within the contour; column (b) shows the results after applying ARAP deformation; (c) shows a triangulation obtained by scattering points within a bounding box, and its deformation result using ARAP; and (d) shows S' after boundary recovering. (For interpretation of the references to color in this figure legend, the reader is referred to the web version of this article.)

Note that the computation of $DepDis$ depends on the position of the anchor points which are determined as the dihedral tessellation is input. Therefore, when there is a large number of inputs, we can perform a quick filtering of the input dihedral shapes with the help of Eq. (4). In addition, a difference in the direction of rotation changes the position of the center of the circle, resulting in a change in the rotation path, which in turn affects the calculation of the contour-deployable distance. Users can specify the direction of rotation for one type of shapes.

4.2. Deployable optimization

In this section, a two-step optimization approach is employed to optimize shapes S_1 and S_2 respectively by minimizing their $DepDis(*)$, which consists of two components: $FDD(*)$ and $CDD(*)$. Firstly, S is deformed such that its anchor frame S^f is simultaneously deformed into a specific template S_{min}^t . Subsequently, the deformed S' undergoes a local contour optimization to obtain final shape T satisfying the contour-deployable constraint.

Optimizing frame-deployable distance: This step aims to align the anchor frame S^f with the template S_{min}^t by deformation. However, only the target positions of the four anchor points are known, making it hard to deduce the complete deformed contour shape based on the movements of anchor points and the original geometric information of the contour. Traditional deformation methods rarely succeed in accurately transforming the anchor frame into the target template while preserving the contour features as much as possible. To address this issue, we propose a bounding box-based As-Rigid-As-Possible (ARAP) method to deform the anchor frame. The ARAP method [51] utilizes a point cloud representation and operates on a triangular mesh generated by triangulating points within the contour, ensuring a global shape consistency that mimics the behavior of real objects under deformation, the results are shown in Fig. 6(b).

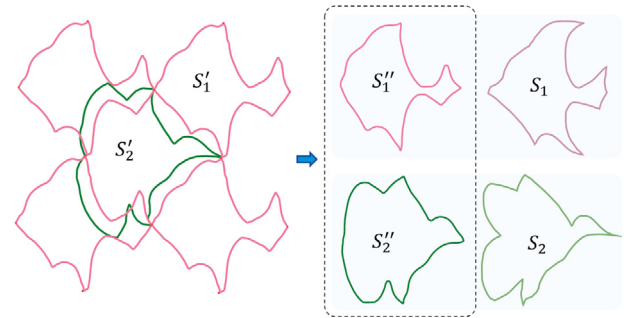


Fig. 7. Shape merging: S'_1 and S'_2 are merged to obtain the interpolated shapes S''_1 and S''_2 .

However, deforming such a mesh by moving the anchor points usually leads to issues, as shown in the green box in Fig. 6(b): triangles near the anchor points undergo significant changes, while internal triangles change very little. This may result in severe distortion or deformation of contour features and, in some cases, even lead to overlapping triangles. While this method achieves satisfactory overall shape deformation, there is still room for improvement in preserving the features of contours, for this reason, the concept of bounding box-based ARAP is introduced.

Different from the typical bounding box determined by the minimum and maximum x and y coordinates, the bounding box used here is expanded outward, leaving a margin width of w_{margin} on all sides. Then triangulate all points including the original contour points and the points scattered in the entire bounding box. Subsequently, the ARAP algorithm is performed and the result is shown in Fig. 6(c).

In comparison to the results in Fig. 6(b), anchor points in the upper green box in Fig. 6(c) still maintain angles after movement without collapsing inward, and in the lower green box, the butterfly's abdomen no longer collapses inward as before. This indicates that the triangles outside the contour within the bounding box act similarly to supports, and the deformation component suffered by the anchor point spreads to the nearby triangles, thus reducing the distortion.

To further preserve the features near anchor points, we propose a boundary recovery method to recover the geometric features around the anchor point, through the local geometric information near the anchor points, as shown in Fig. 6(d). Firstly, the angles $\angle p_{i-t}p_ip_{i+t}$, $t \in [1, t_{max}]$ between the anchor point p_i and the adjacent points p_{i-t} and p_{i+t} on both sides are calculated and recorded before deformation. Here, we recommend setting t_{max} as $0.05 * N$. Based on the difference and direction of the angles before and after the deformation, as well as the Euclidean distance between pairs of points, the points on both side are rotated around the anchor point and translates to the new position. This two-step approach allows for more precise control over the deformation from S_1 , S_2 to S'_1 , S'_2 with better visual appearance.

Optimizing contour-deployable distance: This step aims to deform the dual shapes so that they do not obstruct each other when deployed. Before optimization, S'_1 and S'_2 , the results of frame-deployability optimization for S_1 and S_2 , are supposed to be merged. The merged shape S''_1 , S''_2 can be calculated by the interpolation function:

$$S(M) = \lambda * S(A) + (1 - \lambda) * S(B) \quad (5)$$

$S(*)$ represents an contour composed of an ordered set of points, λ is used to adjust the interpolation weight of shape A and B .

This merging process is illustrated in Fig. 7: the anchors of the two shapes are aligned, and the remaining points between two anchor points are always in one-to-one correspondence, and then the positions of the merged points are calculated according to the above Eq. (5). The general merged result is S''_1 , and the dual shape S''_2 is obtained by recombining the four edges.

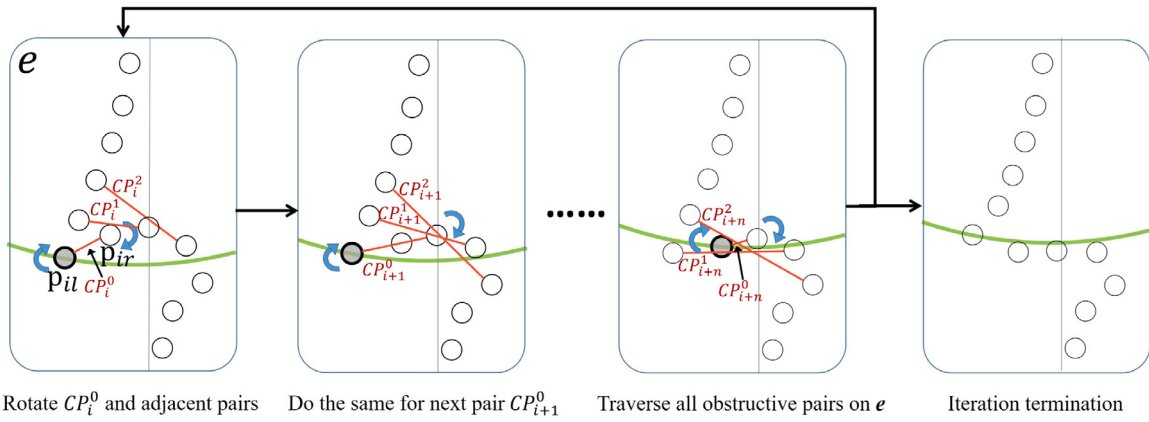


Fig. 8. We detect each collided pair $CP_i(p_{il}, p_{ir})$ of points p_{il} and p_{ir} , calculate the angle θ_i between their connecting line and the tangent line at p_{il} , then rotate this pair CP_i^0 and its neighbor pairs $CP_{i+1}(p_{il-t}, p_{ir+t})$ around each pair's medial point for a certain angle $\alpha_t * \theta_i$, and α_t decreases as t increases. The algorithm stops when there are no more colliding points on the edge or the number of iterations reaches the upper limit.

To find a proper λ that makes the merged result S''_1 and S''_2 to be as similar as possible to the initial shape S_1 and S_2 , we use the following function to measure the similarity between two shapes:

$$Sim(A, B) = \phi(A, B) + \omega(A, B) + Insec(A, B). \quad (6)$$

Here, $\phi(A, B)$ is a shape similarity function based on TAR descriptors, which is introduced in [52]. $\omega(A, B)$ is the area function defined as:

$$\omega(A, B) = Area(A \cap B) / Area(A \cup B). \quad (7)$$

The last item $Insec(A, B)$ is a penalty score to penalize self-intersections in A or B , and the more severe the self-intersections, the lower this value will be in the range $[0, 1]$. We can see that the larger $Sim(A, B)$ is, the higher the similarity between the shapes. Therefore, we would like to find a λ_{max} to maximize the following equation:

$$E_{sim} = \min(Sim(S_1, S''_1), Sim(S_2, S''_2)) \quad (8)$$

When $\lambda = \lambda_{max}$, S''_1 and S''_2 obtain the highest similarity with S_1 and S_2 .

After merging, we provide a deployability optimization method to ensure that the dual shapes satisfy the contour-deployable constraint.

Based on Eq. (3), to minimize the $CDD(S)$, we adopt an iterative method for deployability optimization, as illustrated in Fig. 8. For each edge of the shape, we check each obstructive pair $CP_i^0(p_{il}, p_{ir})$ of points p_{il} and p_{ir} on the edge, calculate the angle θ_i between their connecting line and the tangent line at p_{il} , then rotate this pair CP_i^0 around its midpoint in the direction that decreases the θ_i (clockwise in Fig. 8) for $\alpha_0 * \theta_i$, $\alpha_0 = 0.5$. Then, we rotate the neighbor pairs $CP_i^t(p_{il-t}, p_{ir+t})$ of CP_i^0 around each pair's medial point for a certain angle $\alpha_t * \theta_i$, where $t \in [0, t_{max}]$, $\alpha_t = \alpha_0 / (t + 1)^2$ and here $t_{max} = 0.05 * N$.

Traverse and optimize all the obstructing point pairs CP_{i+n}^0 on the edge and their neighborhoods, and perform the next iteration after the traversal is completed until the number of iterations reaches a predetermined threshold or there are no more obstructive point pairs on the contour.

Note that only optimizing the obstructive point pair CP_i^0 leads to significant cuts or distortions on the contour, so even if the neighboring point pairs $CP_i^t(p_{il-t}, p_{ir+t})$ are not obstructing each other, the algorithm still rotates them so as to ensure the contour to be smooth. On the other hand, when FDD is optimized, the anchor frame will morph into a template and the anchor points will not move again. At this point, a new contradiction arises: if the optimized point pairs are close to the anchor points, the optimization process will rotate the fixed anchor points; if the anchor points are completely fixed and only the other points are moved, it will also lead to severe cuts near the anchor points. To solve this problem, our algorithm further restricts the rotation range of the points near the anchor point based on their distance, i.e., the

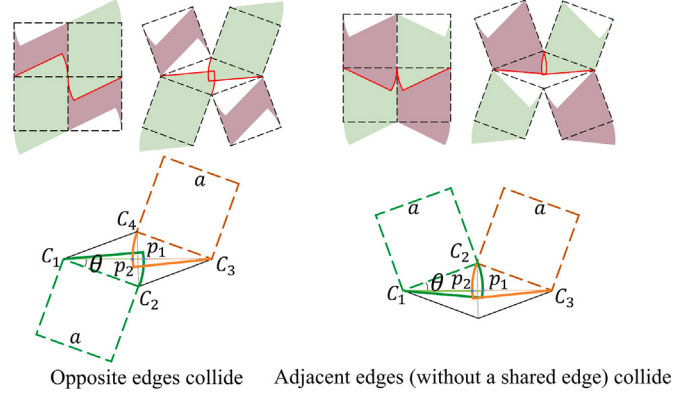


Fig. 9. Collisions may occur on opposite edges (left) or on adjacent edges without a shared edge (right) during deployment, as illustrated by the red lines in the top row. (For interpretation of the references to color in this figure legend, the reader is referred to the web version of this article.)

angle of rotation at each optimization is preceded by the coefficient Δ_{index}/n_e , and Δ_{index} is the subscripted distance from this point to the anchor point.

4.3. Non-adjacent edge deployable optimization

The shape deployability metric function utilized in this paper has been previously introduced. However, this metric function takes into account the degrees of rotational freedom when rotating the units around the axis, which means it only takes into account the deployability optimization of adjacent edges. When deploying our structure, obstructive situations may arise on the other side of neighboring edges or even opposite edges, as illustrated in the top row in Fig. 9.

To detect potential collisions among these edges, the method described in the bottom row of Fig. 9 are employed. For the case of opposite edges, when the rotation angle θ gradually increases from zero as the units deploy, it can be guaranteed that no collision will occur if $length(C_1p_1) + length(C_3p_2)$ is always smaller than the $length(C_1C_3)$, i.e., $length(C_1p_1) + length(C_3p_2) < 2a \cos \theta$, here C_1, C_3 are rotation axis, and p_1, p_2 are the intersections of the line (C_1C_3) and the two units. Similarly, for the case of the other adjacent edges, $length(C_1p_1) + length(C_3p_2) < 2a \cos \theta$ is what we expect.

It is a natural consideration to include all possible obstructing edge pairs in the contour-deployability constraint optimization framework. However, optimizing these non-adjacent edge pairs independently poses a challenge. Only after determining the state of both edges

$$\nu_{xy} = (\nu_{yx})^{-1} = \frac{(a^2 - b^2)(l_2^2 l_1^2 - l_2^4 - A^2) \sin(\theta) + 2ab l_2^2 (l_2^2 + l_1^2 - l_3^2) \sin(\theta + \phi) + 2ab \cos(\theta) \sin(\phi) (l_3^2 l_2^2 - A^2)}{[(a^2 - b^2) \sin(\theta) + 2ab \cos(\theta) \sin(\phi)] A^2} \quad (12)$$

Box I.

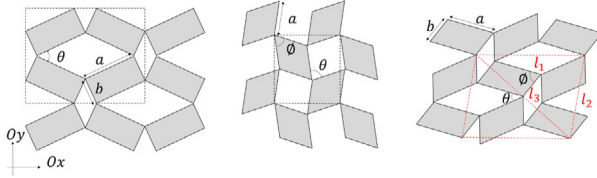


Fig. 10. Negative Poisson's ratio calculations for different types of rotating structures.

can we ascertain whether an obstacle will occur. Consequently, it is difficult to optimize simultaneously to ensure minimal loss of shape features while completely avoiding collisions. To address this issue, we have developed a user interface (UI) that provides an intuitive solution for real-time optimization of these edges while also better preserving boundary features.

4.4. NPR properties analysis

The Poisson's ratio represents the ratio of transverse positive strain to axial positive strain in a material undergoing unidirectional tension or compression. It is an intrinsic property of the material, calculated as

$$\nu = -\frac{\epsilon_{trans}}{\epsilon_{axial}}.$$

In microstructure design, a single material can exhibit vastly different properties through the design of intricate geometries, effectively rendering the periodic structural unit as a new material. Generally, the Poisson's ratio of such a material is not constant, varying with strain and initial geometric parameters. Researchers often employ infinitesimally small strains to calculate the Poisson's ratio for a given state.

Despite the irregular shapes of our auxetic structures, they consistently rotate around the vertices of the anchor frame during deployment. Hence, the overall negative Poisson's ratio property of the structure is intimately tied to the shape of the anchor frame.

According to [1,5,6], it is established that the negative Poisson's ratio of a square rotating structure remains consistently -1. Moreover, as depicted in Fig. 10, the formulas for calculating negative Poisson's ratio values of rotating (semi-)rigid structures with anchor frames shaped as rectangles, rhombuses, and parallelograms are as follows.

Rectangle type I:

$$\nu_{xy} = (\nu_{yx})^{-1} = \frac{a^2 \sin^2(\frac{\theta}{2}) - b^2 \cos^2(\frac{\theta}{2})}{a^2 \cos^2(\frac{\theta}{2}) - b^2 \sin^2(\frac{\theta}{2})} \quad (9)$$

Rhombus type α :

$$\nu_{xy} = (\nu_{yx})^{-1} = \frac{\sin(\frac{\theta-\phi}{2}) \sin(\frac{\theta+\phi}{2})}{\cos(\frac{\theta-\phi}{2}) \cos(\frac{\theta+\phi}{2})} \quad (10)$$

$$= \tan(\frac{\theta-\phi}{2}) \tan(\frac{\theta+\phi}{2}) \quad (11)$$

Parallelogram type I α :

See Eq. (12) in Box I.

These rotating structures have the property of "contraction-expansion-contraction", and will start contracting when the rotation reaches a certain angle, e.g., the square structure starts contracting when the cell rotates more than 45 degrees, while its Poisson's ratio is always -1.

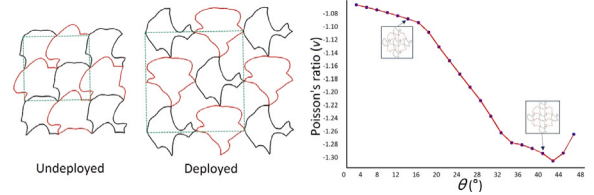


Fig. 11. Negative Poisson's ratio of our structure during deploying.

The rectangular structure starts contracting after an angle greater than 45°, and its Poisson's ratio changes abruptly, i.e., jumps from negative to positive.

Compared to traditional work that focuses on exploring the relationship between material structure and negative Poisson's ratio, this paper places greater emphasis on the utilization of specific negative Poisson's ratio properties. In this paper, different requirements can be met by choosing a specific anchor frame template, such as restricting the anchor frame to be a square to achieve a constant negative Poisson's ratio.

Additionally, our structures are constrained by the boundary correspondence problem, as a result, we investigate the structural properties during the "contract-expand" phase, specifically with a rotation angle of 45°. We also calculate the strain values of the structure at both the initial state and a certain moment during the deploying process. The visual results, as shown in Fig. 11, indicate that the absolute value of the Poisson's ratio of this structure continues to increase during the rotation process and then begins to decrease at approximately 45 degrees, consistent with the these structures with regular units.

5. Results and discussions

We implemented our method and tested it on an Intel Core i7-11700F CPU @ 2.5 GHz and 16 GB RAM. We used a filtered database of about 200 shapes based on [50] to generate suitable dihedral Escher tessellation for a single input pattern.

Performance analysis. When provided with a single shape as input, the algorithm [50] requires at least 20 min to generate a dihedral Escher tessellation. However, with dihedral shapes, our algorithm achieves an average generation time of 13 s for an auxetic dihedral Escher tessellation. The majority of this time is consumed during the two stages of deployability optimization: frame-deployability optimization and contour-deployability optimization. The former, which does not necessitate any iteration, typically completes within 7 s. On the other hand, the latter involves iterative computation of point coordinates, reaching a worst-case time complexity of $O(n^2)$ and averaging 1 s.

Dihedral tessellation comparison. In contrast to traditional Escher dihedral tessellations, our auxetic tessellations adhere to stronger constraints, significantly increasing the challenge of preserving the meaning of the dual shapes. As indicated in Fig. 15, the first row displays the results of optimizing hand-drawn tessellations of Escher into auxetic structures. The subsequent three rows showcase the results of optimizing tessellations generated from a single input pattern. Statistical data for results in this paper are listed in Table 1. It is evident that auxetic tessellations, to some extent, compromise the recognizability of geometric features. Therefore, we utilized AI drawing tools such as Runway and Stable Diffusion to assist us in designing textures,

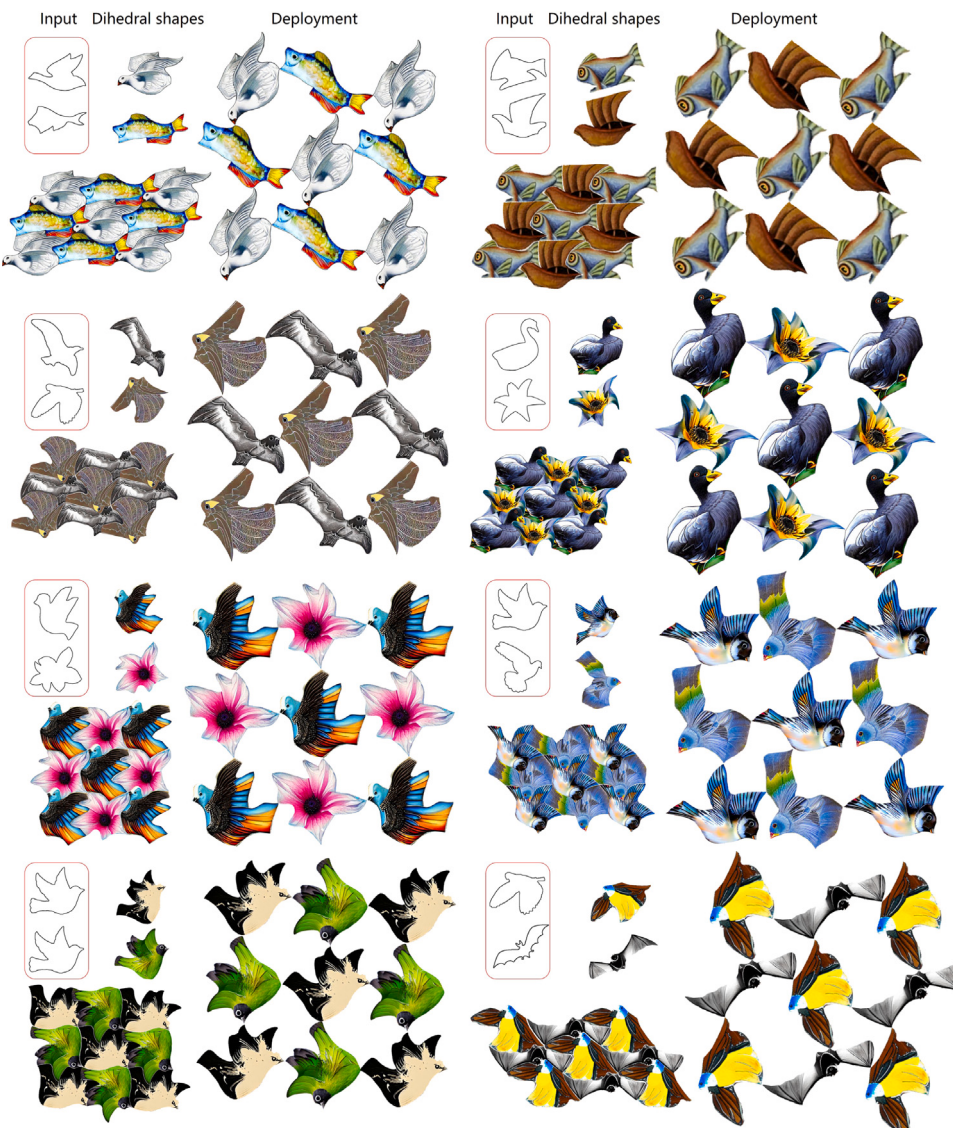


Fig. 12. Joint design for large-scale manufacturing.

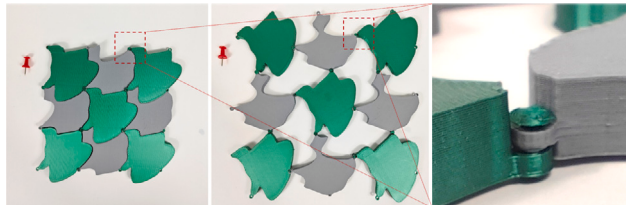


Fig. 13. Auxetic leather tape fabricated through laser cutting.

aiming to enhance both the aesthetic appeal and recognizability of the deployable tessellations.

Fabricated results. Our deployable structures can be designed at various scales for application in diverse decorative scenes. This includes small-scale deployable structures that can be unfolded to fit decorative surfaces in three-dimensional space, such as artistic lampshades, and large-scale deployable structures that can be pre-fabricated and assembled from shape templates. The latter is suitable for application on large-scale artistic curved surfaces, such as screens, windows, and other structures. To accommodate these different scales, we have designed various joints tailored for specific results.



Fig. 14. Stress analysis for triangular rotating (semi-)rigid structure (upper row) and the structure proposed in this paper (lower row). It can be observed that the stress in the triangular structure mainly concentrates at the connections; while in our proposed structure, stress not only concentrates at the connection points but also extends to the tail of the “fish”, surpassing the connection region at the tail. This leads to deformation within the structure during the deploying process.

Table 1

Statistics of the results. S_{min}^t types, FDD, λ and E_{sim} of shape merging, CDD, and total time for optimization are listed, respectively.

Input	S_{min}^t type	FDD	λ	E_{sim}	CDD	Time
Swan&fish	Parall.	0.112	0.45	0.269	0.161	18.2 s
Fish&boat	Rhombus	0.078	0.5	0.181	0.068	18.6 s
Eagle&bird	Parall.	0.070	0.6	0.114	0.236	14.3 s
Duck&flower	Parall.	0.102	0.35	0.186	0.076	15.5 s
Bird&flower	Square	0.035	0.55	0.072	0.217	14.6 s
Two birds I	Parall.	0.018	0.8	0.103	0.565	19.9 s
Two birds II	Rhombus	0.070	0.55	0.121	0.363	15.1 s
Bird&bat	Parall.	0.069	0.3	0.146	0.416	19.6 s

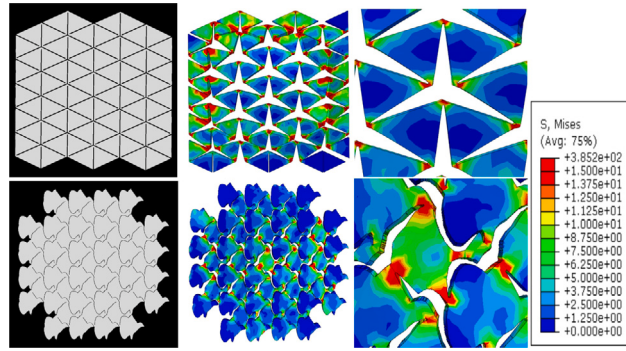


Fig. 15. Auxetic dihedral Escher tessellations. The top row is obtained through deployability optimization on Escher's hand-drawn artwork, while the remaining three rows are based on newly generated dual-shape tessellations.

For large-scale fabrication, a ring structure is added to each unit at the position of the rotation axis. Since there will be four joints stacked together at the same place, the two ring structures come with snaps, which should not be more than 1/2 of the height of the unit. After fabricating by 3D printing, each unit will be placed in the same state as when it was deployed to allow for the combination of joints. After all are assembled, the entire structure can be easily contracted, as shown in Fig. 12.

For small-scale structures, we can generally fabricate them directly through 3D printing or laser cutting, as illustrated in Fig. 13 and right column in Fig. 3. Instead of joints, the units are connected with each other directly, and the rotational movements of the joints can be accomplished with the help of the elasticity and toughness of the materials themselves, such as PLA and leather.

However, this can result in stress concentrations in the connecting parts of the structure, leading to material fracture or fatigue damage, as depicted on the left side of Fig. 14. It becomes necessary to periodically increase the thickness of the joints to ensure the material can withstand numerous “contraction-expansion” processes.

Nevertheless, this solution introduces another challenge: when the connection becomes excessively thick and the material is soft, the concentrated stresses can cause the connection to warp out of plane. This issue is particularly evident in the present work. Upon comparison in Fig. 14, traditional rotating (semi-)rigid structures exhibit regular contours of units, concentrating stresses solely in the connected parts. In contrast, the shape units designed in this paper lead to stress dispersion to other weak areas on the contour, resulting in outward buckling of these regions.

This not only significantly increases the difficulty of driving the deployment of the structure but also leads to serious failure in fully deploying the structure. UI tools can be instrumental in addressing this challenge. By simulating the forces on the structure, users can manually reinforce the weak parts using the UI. Following the modifications, the system will perform a reevaluation to ensure the deployability of the results.

6. Conclusion

In conclusion, our study focuses on enhancing the aesthetics and deployability of rotating auxetic structures. We propose a deployability optimization algorithm that incorporates meaningful contours and Escher tessellations to address the challenges of preserving rotational degrees of freedom while ensuring deployability. Our algorithm is versatile, capable of handling existing tessellations and single input shapes, resulting in manufacturable products with practical utility.

Our contributions encompass the framework for deforming dihedral shapes into auxetic tessellations, the deployability metric function, and the integration of aesthetics with rotating (semi)-rigid structures. We believe that this work represents an effort to unlock new design possibilities and applications in both artistic and practical domains, thereby advancing the field of deployable structures.

Our method does have limitations. While our auxetic tessellations boast interesting and richly meaningful contours compared to the rotating (semi)-rigid structures of regular geometric units, we acknowledge that we sacrifice a portion of the range of rotation. Moreover, in contrast to triangular rotating structure of [10], our quadrilaterals rotating rigid structures exhibit a significantly lower degree of rotational freedom and a reduced ability to approximate the curvature of surfaces. This limitation arises from the structural difference: in triangular structure, six units form a ring, allowing a part of the units to rotate when another part is fixed. In contrast, in quadrilaterals, when any unit undergoes a rotation, the entire structure theoretically have to rotate simultaneously. Thus, relying on the properties of our structure, we can only approximate a developable surface or, relying on the elasticity of the material, approximate some surfaces of lower curvature. Additionally, our method still requires manual optimization of non-adjacent edges, incurring significant manual effort despite preserving features more effectively. Due to the deployability constraint, we impose stricter requirements on the position of anchor points (i.e. the arrangement position of the dihedral patterns), resulting in a smaller solution space compared to traditional Escher dihedral tessellations.

In terms of future work, our plan is to tackle the aforementioned limitations. Additionally, exploring the scalability of the proposed auxetic structures to a larger scale, as discussed in [53], presents an intriguing direction. Another avenue for future research involves enhancing the design of shapes for the unfolded gaps to make them more visually appealing. Currently, each void space comprises two identical pairs of edges, which restricts the range of shapes that can be accommodated. Investigating innovative designs for these gaps could expand the aesthetic possibilities of the algorithm.

CRediT authorship contribution statement

Xiaokang Liu: Conceptualization, Investigation, Software, Validation. **Lin Lu:** Methodology, Supervision. **Lingxin Cao:** Methodology, Software. **Oliver Deussen:** Methodology. **Changhe Tu:** Funding acquisition, Supervision.

Declaration of competing interest

The authors declare that they have no known competing financial interests or personal relationships that could have appeared to influence the work reported in this paper.

Data availability

Data will be made available on request.

Acknowledgments

We thank all the anonymous reviewers for their valuable comments and constructive suggestions. This work is supported by the grant No. 61972232 from National Natural Science Foundation of China (NSFC) and the Key Research and Development Plan of Shandong Province of China (No. 2020ZLYS01).

References

- [1] J.N. Grima, K.E. Evans, Auxetic behavior from rotating squares, *J. Mater. Sci. Lett.* 19 (2000) 1563–1565.
- [2] J.N. Grima, A. Alderson, K.E. Evans, Negative Poisson's ratios from rotating rectangles, *Comput. Methods Sci. Technol.* 10 (2) (2004) 137–145.
- [3] J.N. Grima, K.E. Evans, Auxetic behavior from rotating triangles, *J. Mater. Sci.* 41 (10) (2006) 3193–3196.
- [4] J.N. Grima, V. Zammitt, R. Gatt, A. Alderson, K. Evans, Auxetic behaviour from rotating semi-rigid units, *Phys. Status Solidi (b)* 244 (3) (2007) 866–882.
- [5] J.N. Grima, P.-S. Farrugia, R. Gatt, D. Attard, On the auxetic properties of rotating rhombi and parallelograms: A preliminary investigation, *Phys. Status Solidi (b)* 245 (3) (2008) 521–529.
- [6] D. Attard, E. Manicaro, J.N. Grima, On rotating rigid parallelograms and their potential for exhibiting auxetic behaviour, *Phys. Status Solidi (b)* 246 (9) (2009) 2033–2044.
- [7] J.N. Grima, E. Manicaro, D. Attard, Auxetic behaviour from connected different-sized squares and rectangles, *Proc. R. Soc. A: Math., Phys. Eng. Sci.* 467 (2126) (2011) 439–458.
- [8] G.P. Choi, L.H. Dudte, L. Mahadevan, Compact reconfigurable Kirigami, *Phys. Rev. Res.* 3 (4) (2021) 043030.
- [9] K. Warisaya, H. Hamanaka, A. Tokolo, T. Tachi, Auxetic structures based on rhombic tiling, in: International Design Engineering Technical Conferences and Computers and Information in Engineering Conference, Vol. 85451, American Society of Mechanical Engineers, 2021, V08BT08A031.
- [10] M. Konaković, K. Crane, B. Deng, S. Bouaziz, D. Piker, M. Pauly, Beyond developable: computational design and fabrication with auxetic materials, *ACM Trans. Graph.* 35 (4) (2016) 1–11.
- [11] M. Konaković-Luković, J. Panetta, K. Crane, M. Pauly, Rapid deployment of curved surfaces via programmable auxetics, *ACM Trans. Graph.* 37 (4) (2018) 1–13.
- [12] C. Rao, L. Tian, D.-M. Yan, S. Liao, O. Deussen, L. Lu, Consistently fitting orthopedic casts, *Comput. Aided Geom. Design* 71 (2019) 130–141, <http://dx.doi.org/10.1016/j.cagd.2019.04.018>.
- [13] C. Jiang, F. Rist, H. Wang, J. Wallner, H. Pottmann, Shape-morphing mechanical metamaterials, *Comput. Aided Des.* 143 (2022) 103146.
- [14] A. Rafsanjani, D. Pasini, Bistable auxetic mechanical metamaterials inspired by ancient geometric motifs, *Extreme Mech. Lett.* 9 (2016) 291–296.
- [15] T. Chen, J. Panetta, M. Schnaubelt, M. Pauly, Bistable auxetic surface structures, *ACM Trans. Graph.* 40 (4) (2021) 1–9.
- [16] L.J. Gibson, M.F. Ashby, G. Schajer, C. Robertson, The mechanics of two-dimensional cellular materials, *Proc. R. Soc. Lond. Ser. A Math. Phys. Eng. Sci.* 382 (1782) (1982) 25–42.
- [17] R. Lakes, Deformation mechanisms in negative Poisson's ratio materials: structural aspects, *J. Mater. Sci.* 26 (1991) 2287–2292.
- [18] D. Prall, R. Lakes, Properties of a chiral honeycomb with a Poisson's ratio of −1, *Int. J. Mech. Sci.* 39 (3) (1997) 305–314.
- [19] J.N. Grima, R. Gatt, Perforated sheets exhibiting negative Poisson's ratios, *Adv. Eng. Mater.* 12 (6) (2010) 460–464.
- [20] D. Attard, J.N. Grima, A three-dimensional rotating rigid units network exhibiting negative Poisson's ratios, *Phys. Status Solidi (b)* 249 (7) (2012) 1330–1338.
- [21] Y. Li, Q. Zhang, Y. Hong, J. Yin, 3D transformable modular Kirigami based programmable metamaterials, *Adv. Funct. Mater.* 31 (43) (2021) 2105641.
- [22] R. Gatt, L. Mizzi, J.I. Azzopardi, K.M. Azzopardi, D. Attard, A. Casha, J. Briffa, J.N. Grima, Hierarchical auxetic mechanical metamaterials, *Sci. Rep.* 5 (1) (2015) 8395.
- [23] J.N. Grima, R. Gatt, B. Ellul, E. Chetcuti, Auxetic behaviour in non-crystalline materials having star or triangular shaped perforations, *J. Non-Crystalline Solids* 356 (37–40) (2010) 1980–1987.
- [24] A. Slann, W. White, F. Scarpa, K. Boba, I. Farrow, Cellular plates with auxetic rectangular perforations, *Phys. Status Solidi (b)* 252 (7) (2015) 1533–1539.
- [25] N. Pagliocca, K.Z. Uddin, I.A. Anni, C. Shen, G. Youssef, B. Koobbor, Flexible planar metamaterials with tunable Poisson's ratios, *Mater. Des.* 215 (2022) 110446.
- [26] M. Morvaridi, G. Carta, F. Bosia, A.S. Gliozi, N.M. Pugno, D. Misseroni, M. Brun, Hierarchical auxetic and isotropic porous medium with extremely negative Poisson's ratio, *Extreme Mech. Lett.* 48 (2021) 101405.
- [27] L. Mizzi, K.M. Azzopardi, D. Attard, J.N. Grima, R. Gatt, Auxetic metamaterials exhibiting giant negative Poisson's ratios, *Phys. Status Solidi (RRL)-Rapid Res. Lett.* 9 (7) (2015) 425–430.
- [28] S. Shan, S.H. Kang, Z. Zhao, L. Fang, K. Bertoldi, Design of planar isotropic negative Poisson's ratio structures, *Extreme Mech. Lett.* 4 (2015) 96–102.
- [29] C. Schüller, R. Poranne, O. Sorkine-Hornung, Shape representation by zippables, *ACM Trans. Graph.* 37 (4) (2018) 1–13.
- [30] Y. Ren, J. Panetta, T. Chen, F. Isvoranu, S. Poincloux, C. Brandt, A. Martin, M. Pauly, 3D weaving with curved ribbons, *ACM Trans. Graph.* 40 (ARTICLE) (2021) 127.
- [31] J. Panetta, M. Konaković-Luković, F. Isvoranu, E. Bouleau, M. Pauly, X-shells: A new class of deployable beam structures, *ACM Trans. Graph.* 38 (4) (2019) 1–15.
- [32] S. Pillwein, K. Leimer, M. Birsak, P. Musialski, On elastic geodesic grids and their planar to spatial deployment, *ACM Trans. Graph.* 39 (4) (2020) <http://dx.doi.org/10.1145/3386569.3392490>.
- [33] S. Pillwein, J. Kübert, F. Rist, P. Musialski, Design and fabrication of multi-patch elastic geodesic grid structures, *Comput. Graph.* 98 (2021) 218–230.
- [34] S. Pillwein, P. Musialski, Generalized deployable elastic geodesic grids, *ACM Trans. Graph.* 40 (6) (2021) 1–15.
- [35] C. Jiang, C. Wang, X. Tellier, J. Wallner, H. Pottmann, Planar panels and planar supporting beams in architectural structures, *ACM Trans. Graph.* 42 (2) (2022) 1–17.
- [36] D. Liu, D. Pellis, Y.-C. Chiang, F. Rist, J. Wallner, H. Pottmann, Deployable strip structures, *ACM Trans. Graph.* 42 (4) (2023).
- [37] C. Zheng, T. Sun, X. Chen, Deployable 3D linkages with collision avoidance, in: *Symposium on Computer Animation*, 2016, pp. 179–188.
- [38] Y. Ren, U. Kusupati, J. Panetta, F. Isvoranu, D. Pellis, T. Chen, M. Pauly, Umbrella meshes: elastic mechanisms for freeform shape deployment, *ACM Trans. Graph.* 41 (ARTICLE) (2022) 1–15.
- [39] D. Schattschneider, et al., *Visions of symmetry: Notebooks, periodic drawings, and related work of MC Escher*, vol. 8, WH Freeman, New York, 1990.
- [40] A.W. Dress, The 37 combinatorial types of regular "heaven and hell" patterns in the euclidean plane, in: *MC Escher: Art and science*, Elsevier North-Holland, 1986, pp. 35–43.
- [41] B. Grünbaum, G.C. Shephard, *Tilings and Patterns*, Courier Dover Publications, 1987.
- [42] C.S. Kaplan, D.H. Salesin, Escherization, in: *Proceedings of the 27th Annual Conference on Computer Graphics and Interactive Techniques*, 2000, pp. 499–510.
- [43] C. Kaplan, D. Salesin, Dihedral escherization, in: *Proceedings of Graphics Interface 2004*, in: *GI 2004, Canadian Human-Computer Communications Society, School of Computer Science, University of Waterloo, Waterloo, Ontario, Canada*, 2004, pp. 255–262.
- [44] H. Koizumi, K. Sugihara, Maximum eigenvalue problem for escherization, *Graphs Combin.* 27 (2011) 431–439.
- [45] Y. Nagata, S. Imahori, Escherization with large deformations based on as-rigid-as-possible shape modeling, *ACM Trans. Graph.* 41 (2) (2021) 1–16.
- [46] K. Sugihara, Computer-aided generation of Escher-like sky and water tiling patterns, *J. Math. Arts* 3 (4) (2009) 195–207.
- [47] S.-S. Lin, C.C. Morace, C.-H. Lin, L.-F. Hsu, T.-Y. Lee, Generation of escher arts with dual perception, *IEEE Trans. Visual. Comput. Graph.* 24 (2) (2017) 1103–1113.
- [48] J. Yen, C. Séquin, Escher sphere construction kit, in: *Proceedings of the 2001 Symposium on Interactive 3D Graphics*, 2001, pp. 95–98.
- [49] M. Howison, C.H. Séquin, CAD tools for creating space-filling 3D Escher tiles, *Comput.-Aided Des. Appl.* 6 (6) (2009) 737–748.
- [50] X. Liu, L. Lu, A. Sharf, X. Yan, D. Lischinski, C. Tu, Fabricable dihedral Escher tessellations, *Comput. Aided Des.* 127 (2020) 102853.
- [51] T. Igarashi, T. Moscovich, J.F. Hughes, As-rigid-as-possible shape manipulation, *ACM Trans. Graph. (TOG)* 24 (3) (2005) 1134–1141.
- [52] N. Alajlan, M.S. Kamel, G.H. Freeman, Geometry-based image retrieval in binary image databases, *IEEE Trans. Pattern Anal. Mach. Intell.* 30 (6) (2008) 1003–1013.
- [53] X. Liu, C. Li, L. Lu, O. Deussen, C. Tu, Fabricable multi-scale wang tiles, *Comput. Graph. Forum* 41 (5) (2022) 149–159, <http://dx.doi.org/10.1111/cgf.14610>.